JOURNAL OF
Optical Communications
and Networking

Horizontal free-space optical link with CubeISL over 143 km

Jorge Rosano Nonay,[1,*] René Rüddenklau,[1] Andreas Sinn,[2] Jan Paul Jakobs,[1] Jonas Berlitz,[3] Benjamin Rödiger,[1] and Georg Schitter[2]

[1]Institute of Communications and Navigation (IKN), German Aerospace Center (DLR), Münchener Straße 20, Weßling, 82234, Germany
[2]Automation and Control Institute (ACIN), TU Wien, Gusshausstrasse 27-29, Vienna, 1040, Austria
[3]Responsive Space Cluster Competence Center (RSC³), German Aerospace Center (DLR), Eugen-Sänger-Straße 50, 82234, 29328 Faßberg, Germany
*jorge.rosanononay@dlr.de

Received 9 January 2024; revised 20 March 2024; accepted 27 March 2024; published 30 April 2024

Recent advancements in free-space optical (FSO) communications are enabling a breakthrough in satellite miniaturization and data transfer rates. The CubeISL laser communication terminal (LCT), a development of the German Aerospace Center (DLR), is set to showcase inter-satellite links at 100 Mbps and downlinks at 1 Gbps once it launches in 2025. This technology aims to establish itself as the cutting-edge solution for efficient CubeSat communications, delivering high data rates. To validate its capabilities, the terminal underwent rigorous testing in a 143 km FSO link between the astronomical sites of La Palma and Tenerife in the Canary Islands. The European Space Agency's Optical Ground Station emulated downlinks, while the communication between two LCTs simulated inter-satellite links. This paper outlines the current developmental stage of the CubeISL LCT and presents the outcomes of its horizontal link demonstration.

https://doi.org/10.1364/JOCN.518271

1. INTRODUCTION

Advancements in optical communication systems are enabling a remarkable breakthrough in high-bandwidth satellite communication, where rapidly increasing data volumes are phasing out traditional radio frequency (RF) channels. Free-space optical (FSO) links present superior bandwidth capabilities accompanied by fewer regulatory constraints—unlike RF communication, which faces limitations due to the scarcity of available frequency channels. Moreover, for similar data rates, optical systems boast reduced size, weight, and power (SWaP) requirements in comparison to their RF counterparts, facilitating data throughput of gigabits per second (Gbps) even on the most compact satellites.

The concept of optical communications in space traces back to the 1960s; however, achieving a successful downlink remained elusive until 1995 when the Communications Research Laboratory (CRL) demonstrated a data rate of 1 Mbps with the ETS-VI satellite in a geosynchronous equatorial orbit (GEO) [1]. Subsequent milestones included ESA's demonstration of the first unidirectional optical inter-satellite link (ISL) at 50 Mbps in 2001 using the Artemis satellite in GEO and the SPOT-4 satellite in low Earth orbit (LEO) [2]. Bidirectional optical ISLs were first achieved in 2006 between ESA's Artemis and JAXA's OICETS satellites [2]. Since then, the focus of FSO laser communications has evolved towards high-data-rate systems for large satellites, exemplified by a 5.6 Gbps ISL in 2008 with two of Tesat's laser communication terminals (LCTs) [3]. The rising initiatives by companies and organizations like Starlink, building satellite mega-constellations for global telecommunications, are pushing the development of commercial LCTs for direct-to-Earth (DTE) links and ISLs [4]. Enterprises like Tesat-Spacecom or Mynaric already offer compact satellite terminals for FSO applications.

However, a recent surge in demand for high-speed links on CubeSats has triggered a shift in this trend, boasting significant advancements in miniaturized FSO terminals. The National Institute of Information and Communications Technology (NICT) led the way in 2014 by integrating an LCT in a microsatellite on the SOCRATES mission, achieving a transmission rate of 10 Mbps on a LEO-to-ground link [5]. NASA's OCSD program extended this progress with the development of AeroCube-7B and -7C, two 1.5U CubeSats that achieved optical downlinks of 200 Mbps in 2018 [6]. Remarkably, these vehicles did not necessitate an uplink beacon, relying only on their star tracker and attitude control system for stable satellite pointing. The most significant achievement was reached in 2022 with MIT Lincoln Laboratory (MIT LL) and NASA's TBIRD demonstrating 200 Gbps DTE links from a

6U CubeSat in LEO [7], transmitting over 1 TB of error-free data in a single pass.

The German Aerospace Center's Institute of Communications and Navigation (DLR-IKN) also has a distinguished history in designing laser communication terminals for small satellites in LEO [8]. As part of its Optical Space Infrared Downlink System (OSIRIS) program, the institute developed the OSIRIS4CubeSat (O4C) LCT with a downlink speed of 100 Mbps. In a landmark achievement in 2023, it successfully transmitted an image from the satellite's camera to an optical ground station (OGS). Leveraging modular technology from O4C, DLR-IKN is currently developing CubeISL—a laser communication payload for LEO capable of bidirectional DTE and inter-satellite links. CubeISL is specifically engineered to address the growing need for bandwidth on small satellites in LEO. The enhanced LCT aims for downlinks at 1 Gbps, uplinks exceeding 10 Mbps, and 100 Mbps ISLs at distances of up to 1500 km. Scheduled for a 2025 mission led by DLR's Responsive Space Cluster Competence Center (RSC^3), two 6U CubeSats equipped with an LCT will validate CubeISL's performance.

This paper provides an overview of the current development stage, explores the technological challenges surmounted, and outlines an inter-island link, quantifying the atmospheric aberrations encountered along the horizontal path. Furthermore, it presents comprehensive results concerning the tracking performance between the two ISL terminals and with the OGS.

2. SYSTEM DESIGN AND MISSION ARCHITECTURE

The CubeISL payload is structured into three distinct modules: the optical amplifier, the optical block, and the data and interface module. This modular approach facilitates simultaneous development, testing, and integration of multiple subsystems. Each block occupies around one-third of a unit, as illustrated in Fig. 1, conforming to the CubeSat standard with a total volume of 1U.

The optical amplifier module integrates a commercial off-the-shelf (COTS) erbium-doped fiber amplifier (EDFA) (GOA-1550-S310a, Bktel, France), boasting a maximum output of 1.3 W. To assess its performance at the payload's end-of-life (EOL), the EDFA underwent irradiation with 23 krad(Si) total ionizing dose (TID) using a Gamma-ray source. Consequently, its electrical power consumption increased by 25%, amounting to less than 15 W [9].

Meanwhile, the data and interface module encompass the power distribution and control interface (PDCI) alongside a COTS data handling unit (DHU) (Q8S, Xiphos, Canada). This DHU grants the terminal nearly complete independence from the satellite and offers considerable flexibility for user-defined data processing, encoding, decoding, and storage. Via its high-speed Ethernet and LVDS interfaces, it exchanges data with the satellite's on-board computer (OBC) at 100 Mbps, enabling storage of up to 2 Tbit of information. Moreover, it supports encoding or decoding data with multiple forward error correction (FEC) codes (e.g., Reed-Solomon or low-density parity-check codes).

The optical block, as depicted in Fig. 2, forms the backbone of the CubeISL terminal, utilizing the same optical path for both emitted (red) and received (blue) beams. The optical path starts with a Keplerian beam expander featuring a 20 mm clear aperture (L_{TL1}) and a 7.3 magnification. Subsequently, a fast steering mirror (FSM) (A8L2.2-5000 AU, Mirrorcle Technologies, USA) displaces the incoming beam by up to $\pm 5.2°$, translating to a $\pm 1.0°$ angular offset behind the aperture. The light then passes through the chromatic beamsplitter BS_1, coupling the emitter along the same optical path as the incoming beam. It undergoes focusing, filtering, and splitting by a 30 T/70 R achromatic beamsplitter BS_2. The transmitted portion from BS_2 is used for the tracking loop, where a COTS 1 mm quadrant photodiode (QPD) (G6849-01, Hamamatsu, Japan) and microcontroller measure the beam's offset from the QPD's center and rectify the alignment at a 200 Hz closed-loop bandwidth with the FSM. The system's long focal length ensures high resolution to compensate for minute offsets on the order of a few µrad and minimize pointing losses. The reflected beam at the BS_2 is focused once more by a second focusing lens L_{FL2} that can be adjusted manually in three axes. This design allows simultaneous positioning of the spot at the center of the QPD and on the 200 µm avalanche photodiode (APD). The

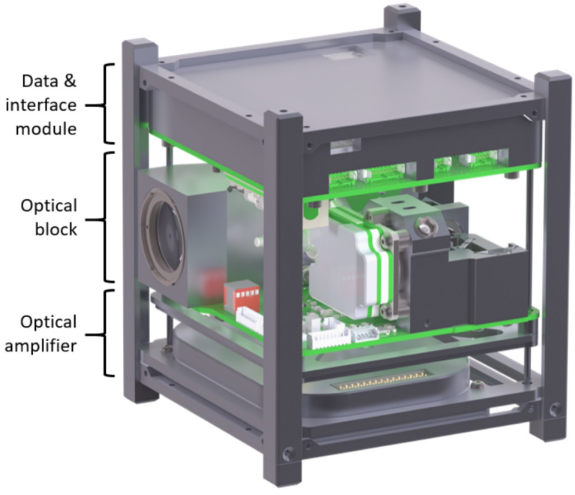

Fig. 1. Model of the CubeISL LCT.

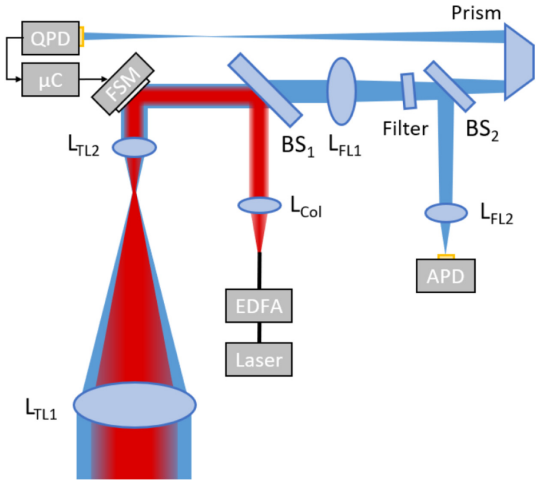

Fig. 2. Schematics of the optical block. The red and blue paths depict the transmitted and received beam, respectively.

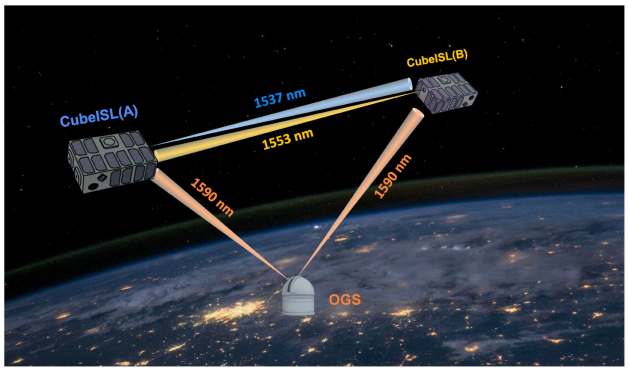

Fig. 3. In-orbit architecture of the CubeISL mission.

APD detector requires a sensitivity of ∼1000 photons per bit to achieve 100 Mbps data readout.

The optical system in Fig. 2 is designed to spectrally isolate the received beam (Rx) of a few nanowatts from the 1.3 W emitted beam (Tx). Employing emitted and received wavelengths 17 nm apart ensures that an OD9 suppression of the emitter's wavelength is possible along the Rx path. However, achieving spectral isolation requires two terminal configurations with opposing wavelengths: CubeISL(A) emits at 1537 nm and receives at 1553 nm, whereas CubeISL(B) emits at 1553 nm and receives at 1537 nm. Consequently, each terminal can only communicate with a terminal of the opposite type. Both CubeISL terminals are designed to receive light at 1590 nm along the same optical path as the one used for OISLs (see blue path in Fig. 2), complying with the new Consultative Committee for Space Data Systems (CCSDS) standard for optical systems [10]. The development of custom beamsplitters and narrowband filters made it possible to combine the two receiver wavelengths and block the transmission wavelength on both terminal configurations. Figure 3 shows the mission architecture for both ISL and DTE links.

One of the primary challenges in an ISL lies in the acquisition procedure between both satellites. Unlike downlinks, where the high-divergence beacon, power, and precise pointing on the OGS simplify the pointing, acquisition, and tracking (PAT) procedure, ISLs with narrower beams and limited power add substantial complexity. CubeISL employs an asymmetrical ISL acquisition scheme, allowing both terminals to independently start without any need for synchronization. As depicted in Fig. 4, each terminal initiates with their respective search patterns, precisely tailored to each other in repetition period and appearance. While both patterns continuously run, the QPD detector samples at 1 kHz to detect any hit events from the opposing LCT. The terminals are distinguished in software as T-PAT (terminal for pointing, acquisition, and tracking) and T-DAT (terminal for detection, adjustment, and tracking). The steps in T-PAT's acquisition pattern are spaced to match the system's divergence, while T-DAT's pattern is adjusted according to the system's field of view. This procedure ensures that within the expected environmental conditions, T-DAT can observe a hit event if the satellites are aligned within each other's field of uncertainty of ±1.0°. Upon a hit, each terminal determines the position error and adjusts its pointing. Subsequently, T-PAT reduces its search pattern while T-DAT

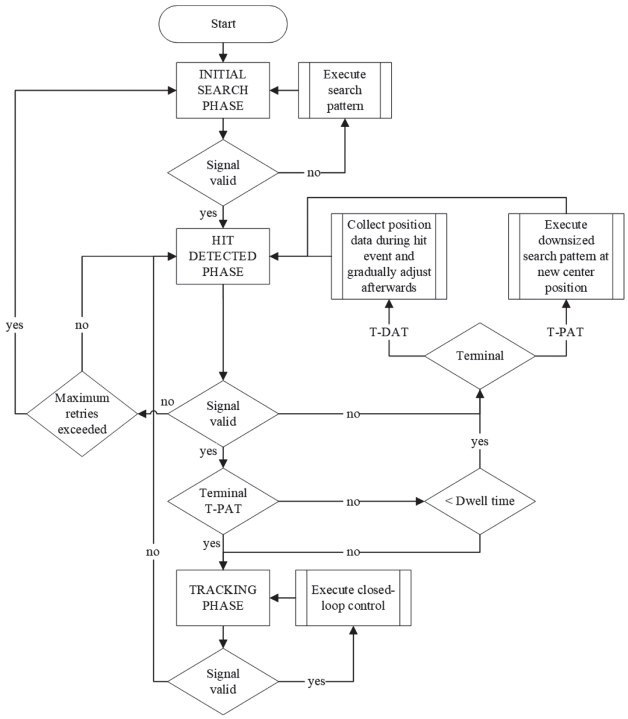

Fig. 4. Flow chart describing the ISL acquisition scheme between the CubeISL(T-PAT) and (T-DAT) configurations.

holds its position, correcting the position with each subsequent hit by the measured position error during the holding phase. If T-DAT receives a constant signal exceeding a specified dwell time, the system switches to closed-loop tracking mode. T-PAT transitions directly to tracking mode upon continued signal presence after the first hit. The holding phase exits after a defined waiting time, reverting to the original search pattern to prevent potential infinite loops due to false positive hits. This acquisition design ensures that even in a constellation where satellites orbit in pairs of type A and B, the software only needs to determine whether to operate as CubeISL(T-PAT) or (T-DAT). This design enables the interchangeability of both terminals and schemes via software.

During DTE links, a beacon from the OGS supports the satellite's fine-pointing, serving as an optical feedback signal for closed-loop tracking. In compliance with the CCSDS standard, the 10 kHz modulated beacon remains distinguishable from static or low-frequency background light perturbations, while remaining detectable by the QPD (beacon tracking) [10]. In ISL scenarios, the terminals initially rely on a 10 kHz sine signal during the PAT procedure. However, when transitioning to data transfer, a single high-frequency signal carries the information for both data transmission and tracking. Although the superimposition of two separate beams is technically feasible, it would complicate the optical system and strain the available link budget, hence not considered. The transmit signal, lying far beyond the QPD bandwidth, appears as a continuous wave (CW) signal, necessitating different processing (CW tracking).

The sensitivity of both tracking methods is primarily limited by thermal and shot noise induced in the QPD and the analog amplifier stages and background noise. Other noise

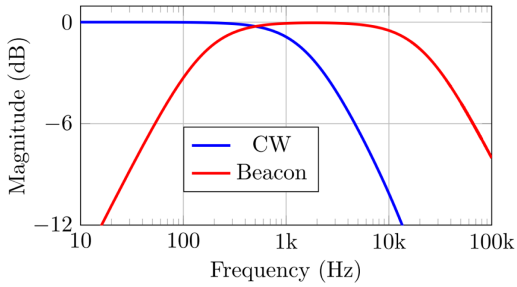

Fig. 5. Frequency response of the beacon and CW tracking schemes on the QPD tracking detector.

contributions (e.g., beacon-to-envelope conversion or signal quantization) are negligible in comparison. To suppress noise outside the transmit frequency bands, signals are lowpass and bandpass-filtered with a 3 dB cutoff set around 22 kHz—for the 10 kHz beacon scenario relevant for the horizontal link campaign (refer to Fig. 5). Overall, the receiver path can be modeled as an additive white Gaussian noise (AWGN) channel, simplifying spot detection as a straightforward Gaussian hypothesis test [11]. The detection threshold is empirically set based on the estimated optical power picked up by the QPD.

In anticipation of the campaign, a hermetic box was built to facilitate effortless transportation, swift assembly, and, if needed, ensure the eye-safe handling of the LCTs. This enclosure accommodates the LCT alongside its emitter—comprising the seed laser and EDFA—and presents a singular aperture designated for the laser beam's emission. For compliance with stringent laser safety protocols, a detachable OD2 filter can be placed over the aperture. Moreover, a 3D-printed interface plate, situated at the rear of the enclosures, features specialized feedthrough channels. These channels enable seamless power supply and facilitate the exchange of essential telemetry with all internal systems. The pragmatic design facilitated the assembly and calibration of the LCTs within a controlled environment at Oberpfaffenhofen, the secure transportation of all delicate components, and expediting operational readiness at the campaign sites within hours. The simple process involved plugging in the necessary interfaces on the box, streamlining the commencement of LCT operations.

3. HORIZONTAL LINK ARCHITECTURE

The 143 km horizontal FSO link was established between the observatories located on La Palma and Tenerife, situated within the Canary Islands archipelago. To establish this link, one CubeISL LCT was positioned at the Jacobus Kapteyn telescope (JKT) in La Palma, while the second LCT was stationed at the ESA OGS in Tenerife, as depicted in Fig. 6. This specific link architecture has been previously utilized in various campaigns, including a record-breaking long-distance quantum entanglement experiment [12]. During the CubeISL campaign, the follwing three successful experiments were conducted.

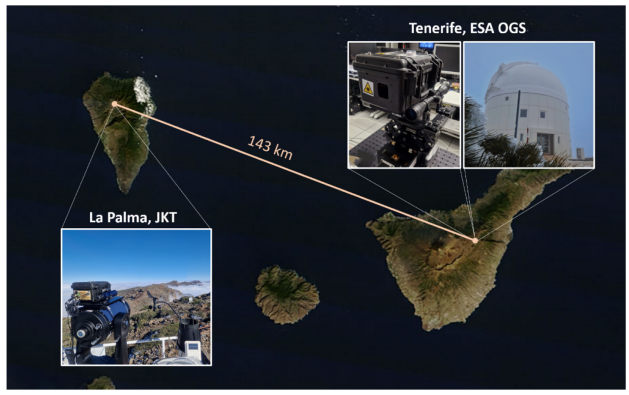

Fig. 6. Architecture of the FSO horizontal link between the JKT at 2369 m and the ESA OGS at 2393 m.

A. OGS Tracking - *Uplink*

This demonstration involved tracking with the LCT on the ESA OGS beacon, effectively simulating an uplink scenario. The primary objective was to showcase the tracking performance of the CubeISL terminal. In this experiment, the beacon installed at the ESA OGS was directed towards the LCT positioned on the neighboring island of La Palma. Despite the challenging 143 km horizontal link, the LCT seamlessly aligned itself with the OGS beacon to establish precise tracking. This link represented a worst-case scenario due to the longer atmospheric path causing increased beam distortion compared to any anticipated uplink conditions on the CubeISL mission. Atmospheric-induced aberrations such as scintillation and attenuation were considered using QCalc, an internally developed tool for computing link budgets [13]. Herewith, the conditions of the 143 km horizontal link were compared to a DTE link between a satellite in orbit at 5° elevation and the OGS in Oberpfaffenhofen, which uses two spatially separated beacons with an aperture diameter of 0.7 cm [14]. The analysis revealed that the attenuation along the horizontal link doubled compared to the DTE link. The scintillation loss on the flat link computed with the Mauna Kea C_2^n model was 2 dB higher than that of the low-elevation DTE link, which was based on the Hufnagel-Valley 5/7 model.

B. Atmospheric Characterization - *Downlink*

Upon establishing dependable tracking between the LCT in La Palma and the OGS beacon, the ESA OGS was used to quantify the atmospheric distortions induced along the horizontal link. Light emitted from the terminal at a wavelength of 1553 nm was harnessed at the Coudé optical bench of the ESA OGS for atmospheric characterization and to evaluate the effectiveness of a tip-tilt compensation mechanism. Sustained precision tracking between the LCT and OGS was crucial to minimize errors originating from emitter pointing, which might otherwise be confused as atmospheric aberrations. Notably, this horizontal experiment is also a representation of worst-case conditions compared to any orbital downlink.

C. Inter-Satellite Tracking - *ISL*

The final experiment achieved the first successful tracking with the CubeISL LCT in an ISL configuration. To the best of the authors' knowledge, this scenario represents one of the farthest FSO links that can be established on ground. In this setup, the LCT in Tenerife remained static and optimally aligned towards the receiving LCT in La Palma. The Tenerife-based LCT utilized its emitter at 1537 nm and 1.0 W, acting as a beacon. Positioned on two elevation and goniometric stages supported by a tripod, this setup facilitated effortless azimuth and elevation adjustments for the terminal's orientation. At the opposite end, the La Palma-based LCT effectively acquired light from the emitter. It maintained reliable tracking for initial pointing offsets up to $\pm 1.0°$, even during night and day, owing to the emitter signal's modulation at 10 kHz. The horizontal experiment and in-orbit ISL are described by the same link budget except for the channel parameters (see Table 2). The higher loss of −18.5 dB in the horizontal link (caused by atmospheric aberrations from attenuation and scintillation effects) is accounted for in orbit by the increased satellite distance of 1500 km. Such an increase in range leads to a loss of −20.7 dB compared to the 143 km horizontal link. Therefore, the horizontal inter-island link can be considered a worst-case scenario for the OISL in orbit.

Prior to the campaign, link budgets were instrumental in validating the viability of each link. Tables 1 and 2 delineate the system parameters and associated link budgets for all three tests. Specifically, Table 2 provides a breakdown comprising emitter (Tx), channel (Ch), receiver (Rx), and budget (Bg) sections.

The emitter section outlines the laser's output power, telescope gain (assuming a truncated, unobscured, and perfectly collimated telescope), component losses, and a pointing penalty. For the LCT, the −2.0 dB pointing loss corresponds to an absolute pointing error of 40 µrad, encompassing misalignment between the emitted and received beams, off-center tracking on the QPD, and atmospheric beam wander. Moving to the channel section, it accounts for quadratic space loss, attenuation, and scintillation losses from the atmosphere. The employed refractive index structure parameter C_n^2 was based on the Mauna Kea model, which aligns better with the conditions in the Canary Islands. To address the saturation regime at very low elevations, where turbulence disrupts light's spatial coherence, a model for strong fluctuations of atmospheric turbulence was employed to determine the scintillation index [15,16]. The downlink scenario, where the OGS serves as the receiver, factors in aperture averaging effects that reduce effective scintillation due to the cancellation of statistical fluctuations caused by the large aperture [17,18]. The scintillation loss after aperture averaging was then computed for a threshold probability of 10^{-3} [19].

For the receiver segment, the telescope gain is determined for both an unobscured LCT and an obscured OGS. It considers the optical loss and splitting loss from its components and beamsplitters, culminating in the available power at the detector surface. Finally, the link margin assesses the difference between detector power and the required power—during tracking, the LCT requires 250 pW (−96.0 dBW) at the detector surface. Both tracking experiments show significant link margins of 30.7 and 7.5 dB, respectively, validating the feasibility of the links with a substantial buffer.

Table 1. Parameters of the Horizontal Link

	Parameter	Unit	Value
LCT	Tx wavelength (La Palma)	nm	1553
	Tx wavelength (Tenerife)	nm	1537
	OOK modulation	kHz	10
	Mean power	W	1.0
	Tx aperture diameter	cm	1.4
	Rx aperture diameter	cm	2.0
OGS	Beacon wavelength	nm	1590
	Beacon OOK modulation	kHz	10
	Beacon power	W	5.0
	Beacon aperture diameter	cm	7.0
	Primary mirror diameter	cm	100
	Secondary mirror diameter	cm	33
Link	JKT altitude	m	2 369
	ESA OGS altitude	m	2 393
	Link distance	km	142.9

Table 2. Horizontal Link Budget[a]

Configuration:		LCT - OGS		LCT - LCT
Experiment:		Uplink Tracking	Downlink	Unidirectional ISL Tracking
Tx	Mean power	7.0	0.0	0.0
	Antenna gain	101.8	88.2	88.2
	Optical loss	−0.5	−0.3	−0.3
	Pointing loss	−1.0	−2.0	−2.0
Ch	Range loss	−241.1	−241.3	−241.4
	Atm. attenuation	−6.7	−7.1	−8.2
	Scintillation loss	−10.2	−2.6	−10.3
Rx	Antenna gain	92.1	125.6	92.2
	Optical loss	−1.5	−2.0	−1.5
	Splitting loss	−5.2	0.0	−5.2
Bg	Power at detector	−65.3	−41.5	−88.5
	Required power	−96.0	–	−96.0
	Link margin	30.7	–	7.5

[a]All values are given in dB.

4. RESULTS

Several refinements to the terminal's design and performance were essential to establish an inter-island link. The optomechanical design enhances the spot quality at the QPD to ensure optimal performance. The tracking sensitivity was evaluated for various modulated signals. Table 2 illustrates a link margin exceeding 3 dB for the ISL tracking scenario. However, achieving this necessitates the LCTs to function consistently at peak performance levels, including high output power and effective suppression of the emitter's signal on the receiving path to avoid self-tracking. These intricate design and performance optimizations are detailed in the following subsection.

A. Terminal Characterization

The terminal's tracking efficiency strongly depends on the size and shape of the spot at the QPD detector plane. Peak sensitivity is achieved with a spot size at the QPD around 60% of the detector's diameter. This relation strikes a delicate balance between coupling losses at the quadrant gaps, tracking range for varying angles of incidence, and positional resolution of the spot across the quadrants. The spot's diameter is adjusted by axial shifts of the focus lens L_{TL1} (see Fig. 2). As the system shares the same path for both the Tx and Rx beams, the axial positioning of the lens also collimates the emitter beam. The system's design theoretically matches optimal collimation and spot size at the same axial position of L_{TL1}. However, in practice, this is not always the case due to manufacturing and integration tolerances. A validation using Zemax OpticStudio demonstrated that any axial displacement of the lens for spot size and tracking sensitivity optimization leads to a threefold improvement in the link budget compared to a similar adjustment to rectify the Tx collimation. For the ISL scenario, prioritizing detector spot size over the system's divergence leads to a higher performance. Consequently, the terminal's Tx beam is first collimated, followed by adjustments to the QPD spot size to align with optical models. Figure 7(a) displays the spot at 1553 nm captured by a short-wave infrared (SWIR) camera, while Fig. 7(b) portrays the simulated spot. The spot's diameter modeled with Zemax at 1553 nm measured 1.00 ± 0.11 mm, closely matching the actual measurement of 0.95 ± 0.03 mm. Similarly, at 1537 nm, the modeled spot of 1.13 ± 0.11 mm correlated well with the measured value of 1.17 ± 0.03 mm.

Additional factors, including the terminal's field of view (FOV), divergence, and detector sensitivity, influence the tracking process and its effectiveness. All these parameters were characterized and integrated into the PAT scheme design. On the CubeISL terminal, the emitter has a $1/e^2$ full divergence angle of ~170 μrad. Its FOV, defined as the angle of incidence (AOI) at the aperture where the beam's chief ray coincides with the detector's border, slightly varies based on FSM position—dependent on the beam's AOI—and wavelength. At 1553 nm and a centered FSM for the FOV, the measured and simulated value stands at 0.7 mrad.

Finally, the receiver's sensitivity significantly impacts tracking performance, primarily influenced by the receiver's electrical design and the modulation type of the emitter signal. The lowest detector power—where tracking remains

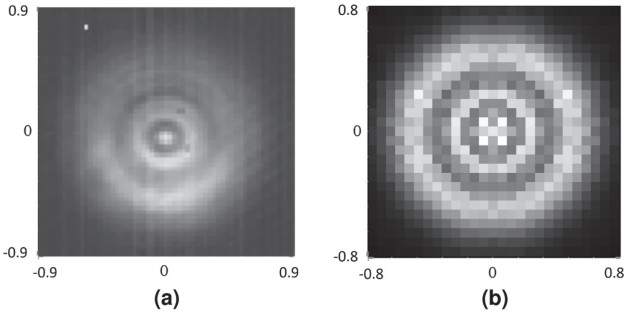

Fig. 7. Comparison of the received spot evaluated 75 mm behind the QPD plane. (a) Measured on LCT. (b) Modeled with OpticStudio.

Table 3. Tracking Threshold for Different Emitters

Emitter Configuration	Power at the QPD, pW
Ideal square	200
Ideal sine	510
Ideal square + EDFA	310
Ideal sine + EDFA	770
Seed laser adjusted sine + EDFA	660

feasible—was determined for multiple 10 kHz beacon configurations. While this evaluation does not represent an absolute characterization of the LCT's minimum power, it provides a relative comparison between different options. The evaluation encompassed two distinctive scenarios: a square and a sine wave signal. Initial tests with an ideal waveform at low power were followed by employing the EDFA at maximum power with subsequent attenuation to assess the amplifier's impact on the waveform. Table 3 summarizes these individual tests, highlighting that an ideal square input signal yields the best performance. The introduction of imperfections to the square signal, possibly due to feeding a sine wave through the system or the dynamic response of the EDFA, led to reduced tracking efficiency. The EDFA, functioning in power-controlled mode, actively follows the commanded signal. The steep slopes when feeding it a square wave signal led to overshoots but still produced superior results compared to an ideal sine wave.

The CubeISL LCT introduces a significant improvement with its output power of 1.3 W (+31 dBm). However, it has been identified that the FSM is deformed (second-order Zernike mode) due to thermal loading, starting at a power of +20 dBm in atmospheric conditions and +17 dBm in vacuum. At +27 dBm, the mirror's surface experiences an instantaneous peak-to-valley defocus, up to 50 nm in ambient conditions and 450 nm in vacuum. This thermal impact can also lead to plastic deformation [20]. To mitigate this, the 5 mm FSMs on the LCT are encapsulated with an inert gas, enhancing static pointing stability and heat dissipation from the mirror's surface. Durability tests conducted at the terminal's highest output power, at 10 kHz and 100 MHz for over 30 min, demonstrated no notable deformation in the beam shape or quality. The devices under test (DUT) showed minimal deviations in the beam's peak power and centroid position—within the system's pointing margin of 40 μrad, as outlined in Table 2. Moreover, second-order Zernike defocus deformations in the mirror could potentially lead to substantial losses in the link budget by increasing transmitter wavefront error (WFE) and beam divergence. Maintaining the total Tx WFE within $\lambda/10$ is crucial to retain WFE losses below −1.7 dB and achieve a beam quality factor M^2 of 1.1, especially given the tight link budget for ISL scenarios at distances of 1500 km. Further tests are planned to assess both the instantaneous elastic deformation of the mirrors at powers of +31 dBm and potential plastic deformations over extended periods of operation.

The high Tx output power also presents a challenge in suppressing light emitted by the terminal from its own detectors; the LCT emits 1.3 W but receives only ~250 pW of power. Unwanted backscattered light can easily saturate the QPD with background noise from the Tx system. To address this,

the system utilizes a bandpass filter with high transmission (>95%) for Rx wavelengths and >OD6 suppression of the Tx wavelength. This filter ensures sufficient isolation of the Tx beam from the receiver along the Rx path. However, during initial testing, the QPD detected and started tracking on its own Tx signal for output powers starting from +20 dBm. The tracking threshold in this experiment for the sum of the 4 QPD pixels was set at 30 counts, where each count (up to 4096) represents a proportional value for the received intensity from the 12-bit signal processed by an internal ADC. A stray-light investigation showed that Tx light was transmitting through the printed circuit board (PCB) of the FSM, reflecting along several external surfaces on the optical block, and infiltrating the QPD through a small gap between the QPD housing and the aluminum block. This issue was resolved by placing a self-adhesive, light-absorbing Acktar coating on selected reflective surfaces and sealing the gap between the QPD housing and the block. With these measures, the backscattered signal on the QPD could be reduced from >30 counts at Tx output powers of +20 dBm to 18 counts for the maximum output power of +31.2 dBm, which is just 6 counts above the noise floor. The iterated design effectively isolates the Tx beam from the system's receivers, ensuring optimal performance for both Tx and Rx systems.

B. Horizontal Link Campaign

Following the comprehensive characterization of the LCT's core functionalities in a controlled setting, the systems were transported and assembled for the horizontal inter-island link test. This test encompassed three experiments: uplink tracking with the LCT on the OGS beacon, transmitting from the LCT to the OGS telescope in a downlink, and unidirectional tracking in an ISL configuration between two LCTs.

1. Tracking Performance with the LCT on the ESA OGS

On the ESA OGS, a fiber laser module generates the beacon signal at 1590 nm. All components of the beacon laser are mounted directly onto the telescope tube of the OGS. Its output is modulated by a square wave signal with a 50% duty cycle and is collimated using a fiber collimator, resulting in a divergence angle of 560 µrad. Two motorized kinematic mirrors enable precise co-alignment of the laser beacon with the OGS telescope. Characteristic landmarks served as reference points at varying distances to support the multi-step alignment process. These landmarks are centered with the OGS using an InGaAs camera. Consequently, the kinematic mirrors are adjusted systematically to align the laser beam's spot with the optical axis of the OGS.

Upon successful alignment of the beacon with the OGS, both were oriented toward the neighboring island and its respective LCT. Their alignment was confirmed using a SWIR camera located in La Palma. Initially, the LCT was roughly aimed toward the OGS beacon using a motorized telescope until its alignment fell within its field of regard (FOR) of ±1 deg. Under these initial conditions, the PAT procedure on the LCT commenced. Links were established and recorded from 04:09 am until the final link at 21:58. Table 4 presents the results for four OGS links conducted under different background lighting conditions. All measurements were carried out in closed-loop tracking mode, where μ_{FSM} represents the normalized offset from perfect alignment. The tracking error itself, σ_{error}, denotes the performance of the LCT. Values smaller than 20 µrad are considered indicative of optimal tracking performance, while those below 40 µrad are still acceptable for operational purposes. Hence, all links met the requirements for data transmission. The last column of the table indicates the impact of wind acting on the LCT, as measured by the onboard gyroscopes.

Table 4. LCT Tracking Performance on the ESA OGS

Scenario	μ_{FSM}, deg	σ_{error}, µrad	σ_{gyro}, $\frac{\mu\mathrm{rad}}{\mathrm{s}}$
OGS 04:09	0.123	3.38	2.09
OGS 17:00	0.123	18.21	15.36
OGS 18:44	0.165	36.40	62.83
OGS 21:58	0.159	12.71	52.36

2. Atmospheric Characterization of the Horizontal Link Path

This experiment evaluates the atmospheric turbulence affecting the horizontal link and explores the potential of tip-tilt compensation to mitigate these disturbances. Figure 8 shows the optical system implemented within the Coudé room of the OGS. The tip-tilt compensation loop comprises a QPD and an FSM, enabling a closed-loop compensation bandwidth of up to 1 kHz through an FPGA-based real-time system. Additionally, a custom-assembled wavefront sensor (WFS) combines a high-speed NIR camera operating at 600 frames per second with a 20 × 20 lenslet array with a 0.36 mm pitch. This configuration enables recording the distribution of higher-order aberrations.

Using the ESA OGS beacon laser, an inter-island link is established with the CubeISL LCT at La Palma. The Tx laser beam from the LCT serves as a reference to conduct measurements using the QPD and the WFS. Figure 9 displays the spatial atmospheric statistics recorded over time using a modal representation captured at 4:57 am. In the first 5 s, without active compensation, a clear dominance of low-order aberrations is visible and indicated by high values at low Zernike indices. By the fifth second, the compensation loop is closed, reducing the tip-tilt RMS errors by up to a factor of 10 from 6.04 µrad and 5.93 µrad to 0.61 µrad and 0.65 µrad, respectively. The total RMS wavefront error decreases by a factor of

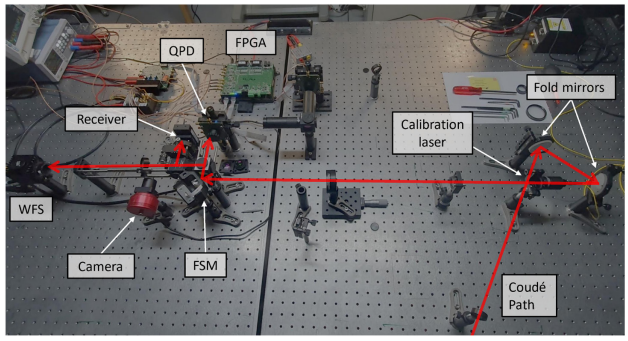

Fig. 8. Setup utilized for atmospheric characterization and tip-tilt compensation within the Coudé room of the ESA OGS.

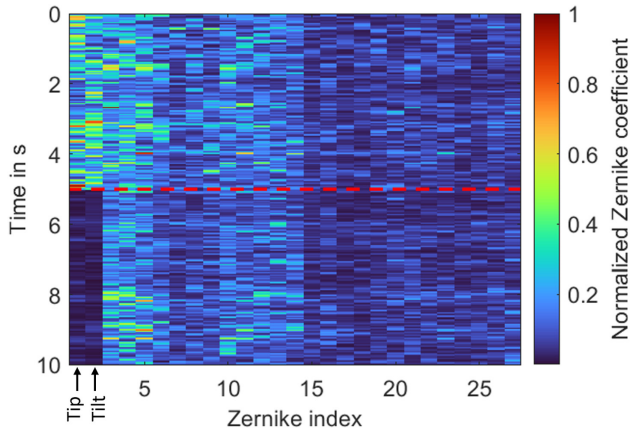

Fig. 9. Measured Zernike distribution over time for the horizontal link. For the initial 0 to 5 s, tip-tilt compensation is disabled. At the 5 s mark (red dashed line), the tip-tilt compensation system is engaged, resulting in a notable reduction in the contribution of tip and tilt aberrations.

1.8, which indicates a 44% contribution of tip and tilt aberrations to the wavefront error. Furthermore, the scintillation index is calculated using the sum signal of the QPD, which is equivalent to the received intensity and is acquired at a rate of 32 kSps. Despite a receiving aperture of 1 m, it reaches the strong scintillation regime with values ranging up to 2.23.

3. ISL Acquisition Pattern for Attitude Error Estimation

The objective of this experiment was to determine the feasibility of estimating residual error using search patterns and, if viable, to assess the accuracy of these results against the tracking reference. This investigation is crucial given that the developed ISL acquisition scheme relies on the assumption that the alignment can be corrected after at least one successful hit, allowing for gradual convergence in the pointing between the two LCTs. However, the absence of an independent angle measurement sensor on its FSM introduces substantial uncertainty into the search process. The hypothesis was tested using data from the unidirectional inter-CubeISL link outlined in Table 5. Due to limited available link time, hindered by thick clouds obstructing the link view, measurements were constrained to a single reference dataset for each acquisition pattern (i.e., grid, spiral, rose, and Lissajous).

Table 5. Unidirectional Tracking Performance with Two LCTs

Scenario	μ_{FSM}, deg	σ_{error}, µrad	σ_{gyro}, $\frac{\mu\text{rad}}{\text{s}}$
ISL 18:17	0.121	29.17	38.40

Figure 10 portrays a comparison of the attitude error estimation between the OGS beacon and the beacon of the second CubeISL terminal. The best results were achieved in both scenarios using the grid pattern, likely attributed to the continuous motion of the system in all other acquisition patterns. The OGS acquisition run started at 16:34, resulting in a measurement error of $1.056 \cdot 10^{-4}$ rad concerning the reference point. Conversely, the ISL link conducted at 19:41 exhibited a deviation of $6.104 \cdot 10^{-5}$ rad between the tracking reference and the attitude derived from the acquisition hits. Both measurements fall within the system's divergence of $\sim 1.7 \cdot 10^{-4}$ rad. Despite atmospheric turbulence and signal attenuation between the islands, the CubeISL LCT demonstrated its capability to acquire, establish, and maintain a link consistently in all experiments involving the ESA-OGS or another CubeISL terminal.

5. SUMMARY AND OUTLOOK

In 2025, two CubeISL payloads are set to demonstrate bidirectional uplinks, downlinks, and ISLs covering distances of 1500 km. The first field campaign successfully confirmed the tracking capabilities of one LCT with an OGS and another LCT. The 143 km horizontal inter-island link between Tenerife and La Palma represented a worst-case scenario, mimicking the ISL and DTE link conditions expected in orbit.

This paper extensively delves into the payload design and tracking architecture of the CubeISL terminal. It meticulously outlines the critical developments that ensured optimal terminal performance before the campaign. These enhancements encompassed spot quality optimization at the detector plane

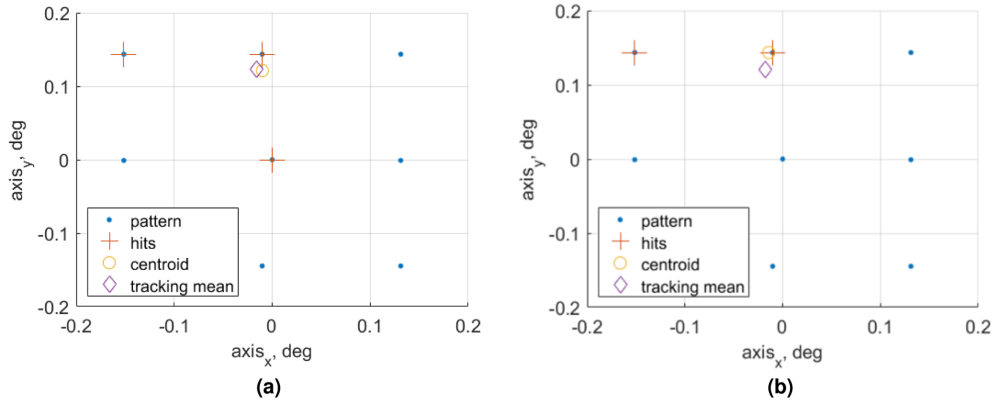

Fig. 10. Comparison of the attitude error estimation during the acquisition phase between an LCT with the OGS and an ISL. The blue dots represent the FSM positions of CubeISL(A) arranged in a grid pattern, with red crosses indicating where a target hit was achieved. The yellow circle depicts the derived centroid position, and the purple diamond, the measured tracking-reference position. (a) CubeISL(A) with OGS beacon. (b) CubeISL(A) with CubeISL(B) beacon.

to align with models within a <5% deviation, stable output power of the Tx signal at 1.3 W, successful isolation of the Tx light from the system's sensors, and comprehensive characterization of multiple emitter configurations and their maximum sensitivity on the detectors. These measures collectively enable tracking Rx signals as low as 200 pW, meeting the necessary performance standards for operations in orbit while providing ample margin for the inter-island tracking between the two LCTs.

The results from the campaign in three key experiments—tracking on an OGS, atmospheric characterization of the link, and tracking on an LCT—affirm the high reliability and performance of the CubeISL payloads. All links established with the ESA OGS confirmed that the PAT procedure remained within the optimal tracking error range (e.g., <20 μrad). Leveraging the Tx signal from the LCT in La Palma, the atmospheric channel along the horizontal link between the islands was characterized. The tip-tilt compensation loop demonstrated a 44% reduction in the contribution of atmospheric aberrations to the signal's wavefront error. Furthermore, the successful verification of assumptions underlying the ISL acquisition scheme was evident in the accuracy of attitude error estimation on the LCT-to-OGS and LCT-to-LCT links. These results showcase the terminal's ability to acquire, establish, and hold a link over 143 km despite atmospheric aberrations.

The upcoming steps in the CubeISL development will focus on establishing a reliable bidirectional link between two LCTs—actively tracking each other—as an end-to-end test of the ISL PAT scheme. Subsequently, following the characterization of the APD data receiver and qualification of its focusing mechanism for space applications, a campaign will validate data transmission at 100 Mbps in an ISL configuration. These pivotal tests will mark the culmination of CubeISL's development, solidifying its position as the world's smallest commercial optical inter-satellite link terminal.

Acknowledgment. The authors thank the IAC for granting access to their telescopes and wavefront sensor equipment, particularly acknowledging the support provided by Jorge Socas, Juan Carlos Perez, and Luis Fernando Rodriguez. Special thanks are extended to Paul Gagern, Anil Morab, Fabian Rein, and Moritz Singer from IKN-DLR for their dedicated assistance in the development of the LCT and to Christian Roubal for his instrumental support in designing the optical subsystem.

REFERENCES

1. K. Araki, Y. Arimoto, M. Shikatani, *et al.*, "Performance evaluation of laser communication equipment onboard the ETS-VI satellite," Proc. SPIE **2699**, 52–59 (1996).
2. S. Kuzkov, Z. Sodnik, and V. Kuzkov, "Laser communication experiments with ARTEMIS satellite," in *Proceedings of the International Astronautical Congress (IAC)* (2013).
3. B. Smutny, H. Kaempfner, G. Muehlnikel, *et al.*, "5.6 Gbps optical intersatellite communication link," Proc. SPIE **7199**, 719906 (2009).
4. A. U. Chaudhry and H. Yanikomeroglu, "Laser intersatellite links in a starlink constellation: a classification and analysis," IEEE Veh. Technol. Mag. **16**, 48–56 (2021).
5. A. Carrasco-Casado, H. Takenaka, D. Kolev, *et al.*, "LEO-to-ground optical communications using SOTA (small optical transponder) – payload verification results and experiments on space quantum communications," Acta Astronaut. **139**, 377–384 (2017).
6. T. S. Rose, D. W. Rowen, S. D. LaLumondiere, *et al.*, "Optical communications downlink from a low-earth orbiting 1.5U CubeSat," Opt. Express **27**, 24382–24392 (2019).
7. C. M. Schieler, K. M. Riesing, B. C. Bilyeu, *et al.*, "TBIRD 200-Gbps CubeSat downlink: system architecture and mission plan," in *IEEE International Conference on Space Optical Systems and Applications (ICSOS)* (2022), pp. 181–185.
8. C. Schmidt, B. Rödiger, J. R. Nonay, *et al.*, "DLR's optical communication terminals for CubeSats," in *IEEE International Conference on Space Optical Systems and Applications (ICSOS)* (2022), pp. 175–180.
9. B. Rödiger, J. R. Nonay, C. Roubal, *et al.*, "Qualification of inter-satellite link laser communication terminals on CubeSats - CubeISL," in *Small Satellite Conference (SmallSat)* (2023).
10. Consultative Committee for Space Data Systems, "Optical communications physical layer," CCSDS 141.0-P-1.1 (2020).
11. C. Grimm, T. Breddermann, R. Farhoud, *et al.*, "Hypothesis test for the detection of moving targets in automotive radar," in *IEEE International Conference on Microwaves, Antennas, Communications and Electronic Systems (COMCAS)* (2017).
12. T. Herbst, T. Scheidl, M. Fink, *et al.*, "Teleportation of entanglement over 143 km," Proc. Natl. Acad. Sci. USA **112**, 14202–14205 (2015).
13. D. Orsucci, J. R. Nonay, A. Shrestha, *et al.*, "QCalc: a tool to compute classical and quantum communication rates over free-space optical channels," Proc. SPIE **11868**, 118680F (2021).
14. A. Mustafa, D. Giggenbach, J. Poliak, *et al.*, "Quantifying the effect of the optimization of an M-fold transmitter diversity scheme with atmospherically induced beam wander and scintillation," in *20th ITG-Fachtagung Photonische Netzwerke* (VDE ITG, 2019).
15. L. C. Andrews and R. L. Phillips, *Laser Beam Propagation through Random Media*, 2nd ed. (SPIE, 2005).
16. N. Das, *Optical Communications Systems* (IntechOpen, 2012).
17. H. Hemmati, *Near-Earth Laser Communications*, 2nd ed., Optical Science and Engineering (CRC Press, 2020).
18. J. R. Nonay, C. Fuchs, D. Orsucci, *et al.*, "SelenIRIS: a Moon-Earth optical communication terminal for CubeSats," in *IEEE International Conference on Space Optical Systems and Applications (ICSOS)* (2022), pp. 186–195.
19. D. Giggenbach and H. Henniger, "Fading-loss assessment in atmospheric free-space optical communication links with on-off keying," Opt. Eng. **47**, 046001 (2008).
20. P. do Vale Pereira, M. Hunwardsen, and K. Cahoy, "Characterization of laser thermal loading on microelectromechanical systems-based fast steering mirror in vacuum," Opt. Eng. **59**, 056109 (2020).